

Light-induced modulation of electrical, optical, and thermodynamic properties via nonlinear phononics in perovskite $KTaO_3$

Qi Yang(杨淇) and Hong Zhang(张红)

Citation: Chin. Phys. B, 2026, 35 (**2**): 026301. DOI: 10.1088/1674-1056/adf5a5
http://cpb.iphy.ac.cn; http://iopscience.iop.org/cpb

What follows is a list of articles you may be interested in

Machine learning-assisted optimization of MTO basis sets

Zhiqiang Li(李志强) and Lei Wang(王雷)
Chin. Phys. B, 2026, 35 (**1**): 016301. DOI: 10.1088/1674-1056/ae0a39

Unveiling the role of high-order anharmonicity in thermal expansion: A first-principles perspective

Tianxu Zhang(张天旭), Kun Zhou(周琨), Yingjian Li(李英健), Chenhao Yi(易晨浩), Muhammad Faizan, Yuhao Fu(付钰豪), Xinjiang Wang(王新江), and Lijun Zhang(张立军)
Chin. Phys. B, 2025, 34 (**4**): 046301. DOI: 10.1088/1674-1056/adb94c

First-principles study of electronic and magnetic properties of self-intercalated van der Waals magnet $Cr_3Ge_2Te_6$

Jia-wan Li(李家万), Shi-Bo Zhao(赵世博), Lin Zhuang(庄琳), and Yusheng Hou(侯玉升)
Chin. Phys. B, 2025, 34 (**3**): 036301. DOI: 10.1088/1674-1056/adab67

Strain-tuned electronic and valley-related properties in Janus monolayers of SWSiX_2 (X = N, P, As)

Yunxi Qi(戚云西), Jun Zhao(赵俊), and Hui Zeng(曾晖)
Chin. Phys. B, 2024, 33 (**9**): 096302. DOI: 10.1088/1674-1056/ad6077

Two-dimensional $Cr_2Cl_3S_3$ Janus magnetic semiconductor with large magnetic exchange interaction and high-T_c

Lei Fu(伏磊), Shasha Li(李沙沙), Xiangyan Bo(薄祥奘), Sai Ma(马赛), Feng Li(李峰), and Yong Pu(普勇)
Chin. Phys. B, 2024, 33 (**9**): 096301. DOI: 10.1088/1674-1056/ad5538

Light-induced modulation of electrical, optical, and thermodynamic properties via nonlinear phononics in perovskite $KTaO_3$

Qi Yang(杨淇)[1] and Hong Zhang(张红)[1,2,†]

[1] *College of Physics, Sichuan University, Chengdu* 610065, *China*

[2] *Key Laboratory of High Energy Density Physics and Technology of Ministry of Education, Sichuan University, Chengdu* 610065, *China*

(Received 23 May 2025; revised manuscript received 18 July 2025; accepted manuscript online 30 July 2025)

Strong long-wavelength laser pulses enable direct manipulation of atomic lattices for engineering novel quantum states in complex materials. Nonlinear coupling between two infrared-active phonon modes (TO_1 and TO_2), induced by intense terahertz light fields, significantly enhances the amplitude of the TO_1 mode and facilitates ultrafast control of transient structural distortions. This light-induced distortion reduces the lattice thermal conductivity from 8.1 $W{\cdot}m^{-1}{\cdot}K^{-1}$ to 3.0 $W{\cdot}m^{-1}{\cdot}K^{-1}$. The reduction originates from the nonlinear coupling, which enhances anharmonic interactions in the lattice potential energy and substantially shortens the phonon lifetime (τ). This work demonstrates a strategy applicable to other perovskite materials and provides a framework for investigating light-induced electrical, optical, and thermodynamic phase transitions.

Keywords: ultrafast processes, ultrafast dynamics, first-principles calculation, phonon–phonon interactions

PACS: 63.20.dk, 63.20.kg, 42.65.Re, 87.15.ht

DOI: 10.1088/1674-1056/adf5a5 **CSTR:** 32038.14.CPB.adf5a5

1. Introduction

$KTaO_3$ crystallizes in a simple cubic perovskite structure with space group $Pm\bar{3}m$ (No. 221) at room temperature. $KTaO_3$ and its derived materials (e.g., solid solutions, nanocomposites) exhibit diverse properties, including piezoelectricity, ferroelectricity, optical properties, superconductivity. These properties drive extensive research for applications in telecommunications,[1] fuel cells,[2] and luminescent capacitors.[3]

Ultrafast laser excitation enables non-equilibrium material control, inducing phenomena such as transient superconductivity,[4–6] high-order harmonic generation,[7] magnetic interaction modulation,[8] and structural/electronic manipulation,[9,10] revealing novel quantum states.[11] These effects are rooted in nonlinear phononic interactions,[12–14] as demonstrated by THz-driven carrier mobility enhancement in K_3C_{60} (metastable superconductivity[15–17]), topological phase transitions in WTe_2,[18] $ZrTe_5$,[19] and graphene,[20] insulator–metal switching in VO_2,[21] and ferroelectric polarization reversal.[22–24] Notably, nonlinear phononics enables hidden-phase induction (e.g., ferroelectricity in $SrTiO_3$[25,26]) and structural transitions,[27,28] advancing ultrafast materials engineering.

Selective excitation of infrared-active phonons enables quantum material control through nonlinear phononics, a low-dissipation approach for manipulating lattice dynamics. Först *et al.* proposed a mode-selective mechanism via ionic Raman scattering,[29–31] where infrared mode excitation drives anharmonic lattice displacements.[32] Chemical doping introduces foreign atoms via substitution, permanently altering chemical composition to modify electronic structure through added charge carriers or defects. This equilibrium state is irreversible by external fields. In contrast, nonlinear phononics uses intense THz pulses to resonantly excite specific infrared-active modes (TO_2), inducing transient displacements in target modes (TO_1) via anharmonic coupling. Energy transfer occurs through coherent lattice vibrations without charge carriers or compositional changes, thus enabling dynamic, reversible control of phonon amplitudes on fs-to-ps timescales. Light's tunable temporal profiles, spectral bandwidths, and polarization states[33] further enhance its precision in ultrafast material engineering.

$KTaO_3$ exhibits high sensitivity to external stimuli such as electromagnetic radiation and strain while maintaining structural stability without any phase transitions from sub-room temperature down to the millikelvin range,[34] making it an ideal platform for investigating nonlinear phonon dynamics and ultrafast optical control. In this work, we modify the lattice structure by driving the lowest-frequency optical phonon mode in incipient ferroelectric $KTaO_3$ into the strongly nonlinear regime via phonon–phonon coupling under intense terahertz excitation. Ultrafast structural control originates from nonlinear coupling between infrared-active phonon modes Q_1 and Q_2. External pumping of the Q_2 mode induces nonlinear distortion along the Q_1 coordinate,[29] leading to symmetry breaking and transient lattice distortion.

[†]Corresponding author. E-mail: hongzhang@scu.edu.cn

© 2026 Chinese Physical Society and IOP Publishing Ltd. All rights, including for text and data mining, AI training, and similar technologies, are reserved.

Combining first-principles calculations with nonlinear phonon theory, this study systematically probes the light-induced evolution of electronic structure, optical properties, and thermodynamic characteristics in $KTaO_3$. The results reveal that TO_1 and TO_2 phonon modes, driven by light-induced dynamical instability, enable synergistic regulation of optical response and thermal transport. This approach exhibits superior tunability and dynamic adaptability, facilitating rapid switching of photothermal properties while preserving structural integrity. Specifically, this work demonstrates three key advances in light-controlled $KTaO_3$: (i) a 62.9% suppression of lattice thermal conductivity via photoinduced structural distortion, superior to chemical doping;[35] (ii) on-demand creation of optical anisotropy through laser-induced symmetry breaking, absent in pristine $KTaO_3$; and (iii) unified control of electronic, optical, and thermal properties via the Q_1 modulation mechanism. Collectively, these findings establish a new paradigm for nonlinear phononic control based on transient lattice distortion, with significant implications for photothermal conversion devices and thermoelectric optimization. The developed methodology provides a theoretical foundation for quantitatively predicting light-matter coupling effects and rationally designing novel functional materials.

2. Computational method

The unit cell of $KTaO_3$ was calculated using density functional theory (DFT) with the projector augmented wave (PAW) method,[36] as implemented in the Vienna *ab initio* simulation package (VASP).[37–39] Our computational study encompassed structural relaxation, phonon dispersion, and calculations of electronic, optical, and thermodynamic properties. For structural optimization, the exchange–correlation functional was treated with the generalized gradient approximation (GGA) using the Perdew–Burke–Ernzerhof (PBE)[40] functional, augmented by DFT-D3 van der Waals corrections.[41] A plane-wave cutoff energy of 520 eV was employed, with the energy convergence threshold set to 10^{-7} eV, and the Brillouin zone sampled using a $12 \times 12 \times 12$ Monkhorst–Pack k-point grid. Phonon calculations were performed within density functional perturbation theory (DFPT) using a $3 \times 3 \times 3$ supercell model via the PHONOPY code,[42] incorporating spin-orbit coupling. Electronic properties were evaluated using the Heyd–Scuseria–Ernzerhof (HSE06) hybrid functional.[43] Optical properties were calculated using the GW approximation for the Green's function and screened Coulomb interaction, coupled with the solution of the Bethe–Salpeter equation (BSE) as implemented in VASP.[44,45] The GW+BSE calculations utilized a $12 \times 12 \times 12$ k-point grid and a GW cutoff energy of 600 eV. Thermodynamic properties were computed using the phono3py program[46] in conjunction with VASP.

3. Results and discussion

3.1. Nonlinear phonon dynamics

The lowest-energy cubic structure of $KTaO_3$ (lattice constant $a = b = c = 4.02$ Å) was optimized using DFT as shown in Fig. 1(a). Phonon frequencies and eigenvectors were computed via density functional perturbation theory (DFPT), including spin–orbit coupling. Due to significant LO–TO splitting, dielectric constants and Born effective charges were incorporated. Since light only excites phonons near the Γ point of the Brillouin zone ($q = 0, 0, 0$), we restricted our analysis to modes belonging to the irreducible representations of the $Pm\bar{3}m$ space group. The calculated phonon modes are listed in Table 1. $KTaO_3$ has four triply degenerate optical phonon modes at the center of the Brillouin zone, and we label these four modes as TO_1, TO_2, TO_3, and TO_4 respectively. TO_1, TO_2, and TO_3 are infrared-active (T_{1u}), while TO_4 is optically inactive (T_{2u}). The nonlinear coupling between TO_1 and TO_2 modes (atomic displacements and vibrational patterns in Fig. 1(b)) is central to this study.

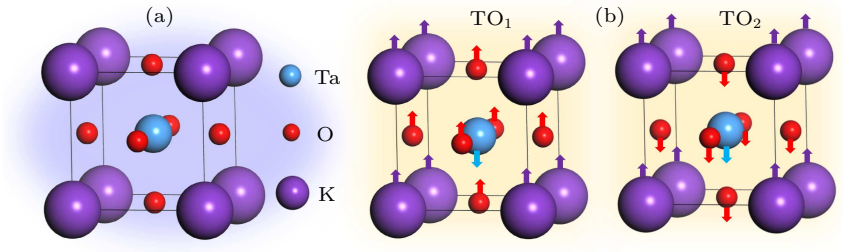


Fig. 1. Structure and polarization configurations in $KTaO_3$. (a) The cubic lattice structure of $KTaO_3$. (b) Schematic representation of atomic displacements corresponding to infrared active modes TO_1 and TO_2 at Γ. The arrow indicates the direction of the phonon displacement.

Table 1. Frequencies of phonon branches at the center of the Brillouin zone for $KTaO_3$.

Phonon branch	Symmetry	Frequency (cm^{-1})	Ref. [34] (cm^{-1})	Ref. [47] (cm^{-1})
TO_1	T_{1u}	31.06	62.7	25
TO_2	T_{1u}	182.93	181.8	196
TO_3	T_{2u}	263.39	216.4	282
TO_4	T_{1u}	516.61	556.6	547

To determine the nature and strength of the coupling between phonons, we performed energy surface calculations based on the amplitudes of these modes. The following expression is provided:

$$\begin{aligned} V(Q) = & \frac{\omega_1^2}{2}Q_1^2 + \frac{\omega_2^2}{2}Q_2^2 + a_1Q_1^4 + b_1Q_2^4 \\ & + a_2Q_1^6 + b_2Q_2^6 + a_3Q_1^8 + b_3Q_2^8 + c_1Q_1Q_2 \\ & + c_2Q_1^2Q_2^2 + c_3Q_1^3Q_2^3 + c_4Q_1^4Q_2^4 \\ & + d_1Q_1Q_2^3 + d_2Q_1^3Q_2 + d_3Q_1^3Q_2^5 \\ & + d_4Q_1^5Q_2^3 + e_1Q_1^2Q_2^4 + e_2Q_1^4Q_2^2 \\ & + e_3Q_1^2Q_2^6 + e_4Q_1^6Q_2^2, \end{aligned} \tag{1}$$

where Q_α ($\alpha = 1,2$) represents the real-space eigen displacements of the infrared-active modes TO_1 and TO_2, and ω_α represents the corresponding eigenfrequency of the phonon modes. The atomic displacements due to an amplitude Q_α is given by $U_j = \frac{Q_\alpha}{\sqrt{m_j}}\omega_j^\alpha$; where U_j is the displacement of the j-th atom, m_j is the mass of this atom, and ω_j^α represents the corresponding component of the TO_1 and TO_2 mode vectors, which is normalized and dimensionless. We use the units of eV for energies, amu for masses, and $\text{amu}^{1/2}\cdot$Å for the normal mode amplitudes Q_α.

Phonon coupling can lead to atomic displacements that deviate from the harmonic potential equilibrium due to anharmonic effects. The calculated energy surface is shown in Fig. 2(a), and the values of the anharmonic constants are listed in Table 2. As depicted in Fig. 2(a), the energy landscape exhibits a unique minimum as a function of the amplitude of the TO_1 mode for a given amplitude value of TO_2. Furthermore, once the amplitude of the TO_2 mode becomes non-zero, TO_1 mode shifts from its equilibrium position. These results demonstrate strong coupling between the TO_1 and TO_2 modes. Such coupling implies that exciting one mode induces a significant response in the other.

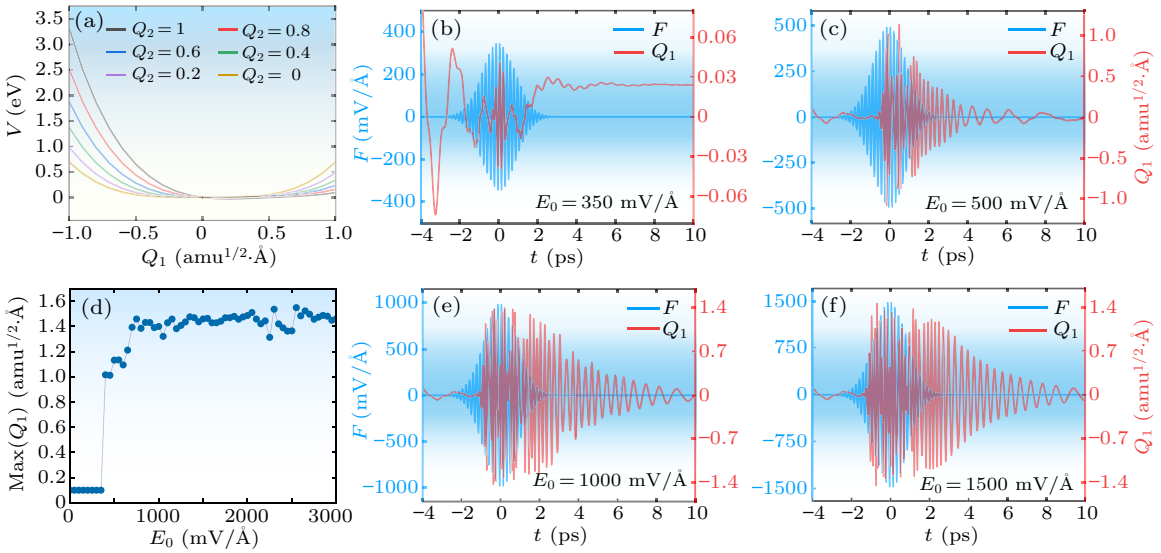


Fig. 2. (a) Total energy as a function of the TO_1 mode amplitude (Q_1) for fixed TO_2 mode amplitudes (Q_2). Q_1 varies from -1 $\text{amu}^{1/2}\cdot$Å to 1 $\text{amu}^{1/2}\cdot$Å. For visual clarity, we plot $V(Q_1,Q_2)$–$V(0,Q_2)$ so that all curves coincide at $Q_1 = 0$. Panels (b), (c), (e) and (f) show the time-dependent dynamics of Q_1 at $E_0 = 350$ mV/Å, 500 mV/Å, 1000 mV/Å, and 1500 mV/Å, respectively. (d) Maximum displacement amplitude of Q_1 as a function of field intensity E_0.

Table 2. The coefficients of the anharmonic, and nonlinear coupling terms of the polynomial used to fit the calculated total-energy surface $V(Q_1,Q_2)$ of $KTaO_3$. The unit of the Q^mQ^n term is $\text{meV}\cdot\text{amu}^{-(m+n)/2}\cdot\text{Å}^{-(m+n)}$.

Coefficient	Order	Cubic	Coefficient	Order	Cubic
ω_1^2	Q_1^2	3.110	c_3	$Q_1^3Q_2^3$	6.446
ω_2^2	Q_2^2	123.715	c_4	$Q_1^4Q_2^4$	128.174
a_1	Q_1^4	955.573	d_1	$Q_1Q_2^3$	–356.705
b_1	Q_2^4	718.916	d_2	$Q_1^3Q_2$	–271.632
a_2	Q_1^6	–61.909	d_3	$Q_1^3Q_2^5$	–19.827
b_2	Q_2^6	–1050.727	d_4	$Q_1^5Q_2^3$	3.343
a_3	Q_1^8	200.712	e_1	$Q_1^2Q_2^4$	–224.578
b_3	Q_2^8	524.747	e_2	$Q_1^4Q_2^2$	–517.482
c_1	Q_1Q_2	27.437	e_3	$Q_1^2Q_2^6$	86.281
c_2	$Q_1^2Q_2^2$	1300.121	e_4	$Q_1^6Q_2^2$	237.912

In order to manipulate the symmetry breaking of $KTaO_3$ via optical excitation and investigate the evolution of anharmonic systems, we further explored the dynamics of nonlinearly coupled modes when the TO_2 mode is externally pumped. In this process, both the TO_1 and TO_2 modes are influenced by the calculated energy surface and an external driving term $F(t)$. Based on these considerations, we derived the dynamical equations describing the motion of the system

$$\ddot{Q} + \gamma\dot{Q} + \nabla_Q\left[V(Q) - F(t)Q_2\right] = 0, \tag{2}$$

$$F(t) = E_0\sin(\omega t)\,\mathrm{e}^{-t^2/2(\sigma/2\sqrt{2\ln 2},)^2}, \tag{3}$$

where Q describes the displacements of Q_1 and Q_2, γ is the damping constant of each mode. $F(t)$ denotes the specific intense THz excitation pulse. where E_0, σ, and ω are the ampli-

tude, full width at half maximum (FWHM), and frequency of the light pulse, respectively. $\omega = \omega_2$, $\sigma = 2$ ps.

Numerical integration of Eq. (2) reveals that the TO_1 phonon mode can be excited in $KTaO_3$ via laser pumping at a central frequency of 5.48 THz. Figure 2 presents the evolution of the infrared-active mode Q_1 under different field strengths: under weak excitation (low pump intensity), Q_1 develops a non-equilibrium displacement, stabilizing the metastable system and asymptotically converging towards the steady-state value. As shown in Fig. 2(b) (field strength set to 350 mV/Å), Q_1 stabilizes at 0.023 amu$^{1/2}\cdot$Å, indicating a small displacement amplitude. When the field strength exceeds 400 mV/Å, Q_1 exhibits oscillation-like behavior (Figs. 2(c), 2(e), 2(f)), with the amplitude decaying to zero following resonant excitation under strong pumping.

To clarify the relationship between $\max(Q_1)$ and the applied THz optical field intensity E_0 in the theoretical calculations, we sampled the range 0 mV/Å–3000 mV/Å in steps of 50 mV/Å (Fig. 2(d)). The results indicate that Q_1 shows almost no oscillation for $E_0 < 400$ mV/Å. Stronger fields trigger enhancement of the TO_1 mode, while $\max(Q_1)$ gradually saturates under high pumping. This nonlinear relationship likely stems from the periodic oscillation of the driving force and phonon damping effects. Figure 2(d) shows that over the range 700 mV/Å–3000 mV/Å, $\mathrm{Max}(Q_1)$ converges to 1.45 ($\pm$0.05) amu$^{1/2}\cdot$Å, demonstrating a field-induced stabilization effect.

Although the theory covers extreme field strengths up to 3000 mV/Å, achieving the intensities shown in Fig. 2(d) presents significant challenges experimentally. Current THz source power output is limited by dielectric breakdown thresholds and energy conversion efficiency. The stable operating range for most experimental systems is concentrated around $E_0 = 100$ mV/Å–1500 mV/Å,[48] showing a considerable gap compared to the upper limit of the theoretical calculations. Therefore, the core focus of experimental validation should lie within the currently achievable range of strong-field THz technology. The pronounced response of $KTaO_3$ within this range provides a basis for verifying the relationship between $\max(Q_1)$ and E_0. At $E_0 = 400$ mV/Å, a displacement of $\max(Q_1) \approx 1$ amu$^{1/2}\cdot$Å can be induced, which falls within the experimentally accessible range, suggesting that theoretical verification can proceed in stages. Experiments must account for nonlinear absorption, lattice distortions, and irreversible damage under strong fields, necessitating the use of cryogenic conditions to suppress thermal effects. Utilizing advanced structural probing techniques offers the potential to clearly confirm the theoretical model experimentally and possibly extend the exploration moderately beyond the current stable field strength limits of experimental technology. Exploration of physics at even higher field strengths will rely on future breakthrough advancements in THz source technology.

3.2. Electronic properties

To investigate material performance in photovoltaic and optoelectronic applications, understanding their electrical properties is crucial. A comprehensive analysis of the light-induced structural transformations in $KTaO_3$ was performed, coupled with first-principles calculations of the pump excited electronic band structure (Fig. 3). The band gap defines the energy range available for electrons in a solid material and serves as a critical parameter for understanding the material's electrical conductivity.[49] The band structure provides essential insights into the energy levels of occupied and unoccupied electronic states, as well as the electronic transitions between the valence and conduction bands in solids. Analysis of the electronic band structure is a fundamental approach in first-principles calculations for elucidating the properties of solid materials.

The valence band maximum (VBM) occurs at the R point, and the conduction band minimum (CBM) at the Γ point of the Brillouin zone. This result demonstrates that $KTaO_3$ exhibits characteristic insulating behavior with an indirect band gap. According to solid-state theory, electron excitation processes are more complex in indirect bandgap materials than in direct bandgap ones. The calculated bandgap of $KTaO_3$ using HSE06 hybrid functional with spin–orbit coupling correction yields 3.91 eV, which shows reasonable agreement with existing theoretical and experimental reports. While this value is slightly higher than the experimental measurement of 3.6 eV,[50] it demonstrates significant improvement over standard PBE functional results (2.1 eV)[51] and aligns well with other advanced computational approaches, including HSE06 (3.44 eV)[52] and TB-mBJ (3.33 eV)[35] methods reported in literature.

Pump excitation induces significant degeneracy lifting in the band structure of $KTaO_3$, manifested as the splitting of the conduction band at the Γ point and the valence band at the R point. At $Q_1 = 0$ (Fig. 3(a)), bands near high-symmetry points Γ and R exhibit high degeneracy. With increasing Q_1 (Figs. 3(b)–3(f)), coherent phonon oscillations directly break the crystal potential symmetry. This causes degenerate energy levels at Γ and R to split into multiple subbands according to the irreducible representations of the new symmetry group. Further analysis reveals that increasing Q_1 enhances the contribution of anharmonic terms in the lattice potential, intensifies phonon–phonon scattering, and shortens phonon lifetimes. Shorter-lived phonons exhibit increased scattering probability with electrons, reducing electron coherence. This ultimately leads to band broadening, reduced band curvature (e.g., flattened slope of the Γ-point conduction band), and enhanced electron effective mass. These symmetry breaking effects significantly alter carrier effective mass and transition dipole moments, thereby modulating the material's electronic and optical properties.

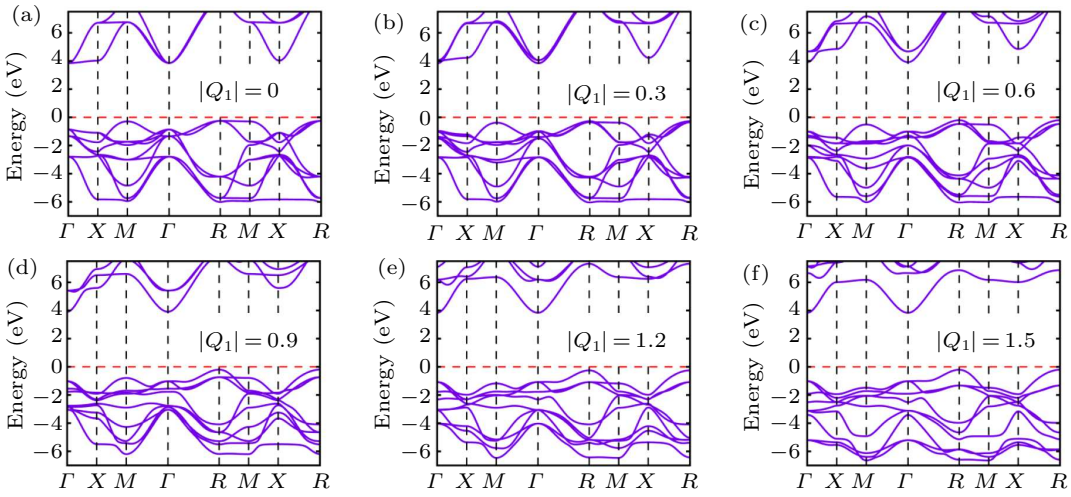


Fig. 3. The band structure of $KTaO_3$ calculated using the HSE06 functional, where panels (a), (b), (c), (d), (e), and (f) correspond to Q_1 values of 0, 0.3, 0.6, 0.9, 1.2, and 1.5 amu$^{1/2}\cdot$Å, respectively.

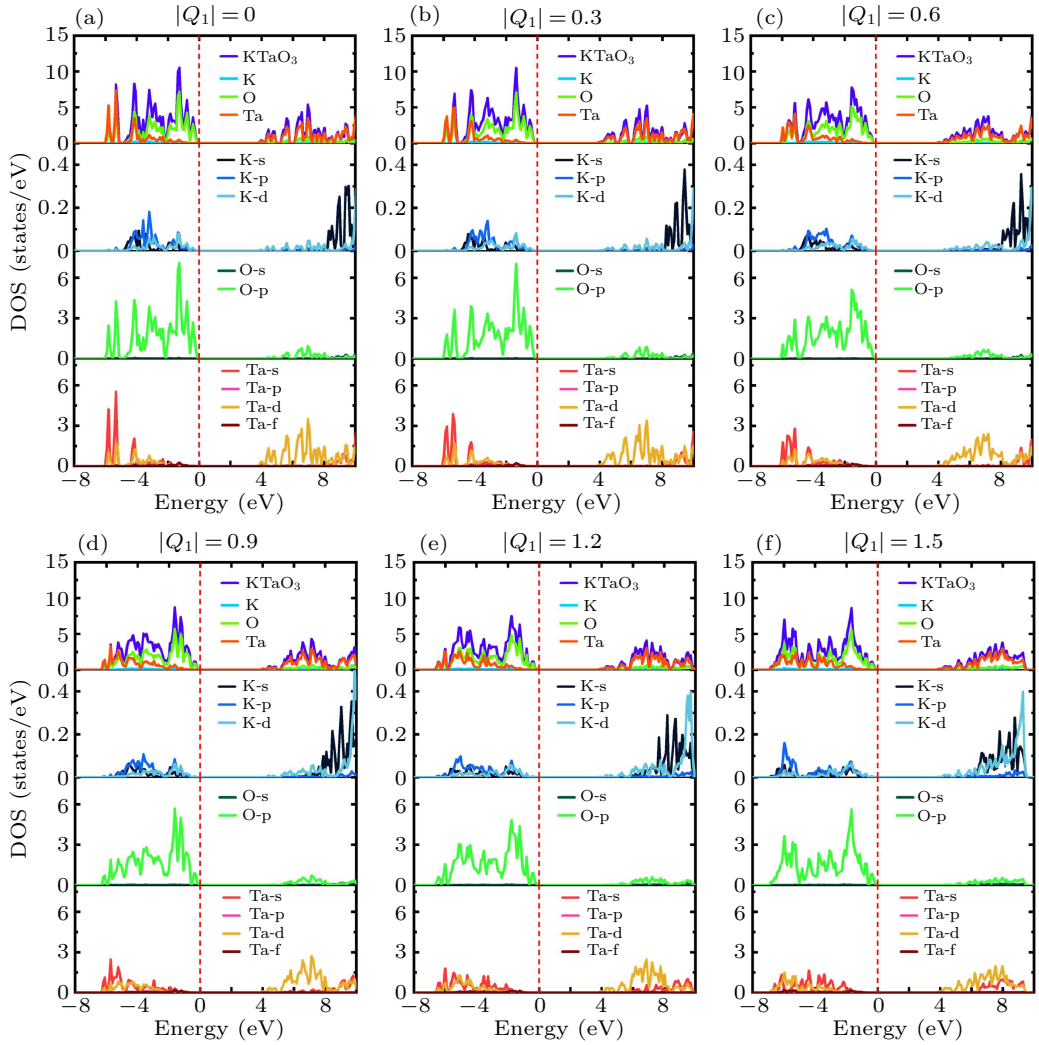


Fig. 4. The densities of states (TDOS and PDOS) of $KTaO_3$ calculated using the HSE06 functional, where panels (a), (b), (c), (d), (e), and (f) correspond to Q_1 values of 0, 0.3, 0.6, 0.9, 1.2, and 1.5 amu$^{1/2}\cdot$Å, respectively.

To examine elemental/orbital contributions and band evolution, we computed the total and partial densities of states (DOS/PDOS). Figure 4 shows the DOS of $KTaO_3$ under varying Q_1 displacements. In pristine $KTaO_3$ (Fig. 4(a)), the valence band is dominated by Ta-s/d and O-p orbitals, while the conduction band comprises Ta-d and O-p states, which is consistent with the findings of Akter *et al.*[53] O-p orbitals persistently govern the Fermi-level region across all configurations,

a hallmark of oxide perovskites.[54]

Notably, pristine $KTaO_3$ exhibits prominent interband transitions between O-p and Ta-d states. With increasing Q_1, lattice distortion disrupts the local coordination environment. This distortion alters the orbital hybridization between Ta-d and O-p states. Consequently, the density of states (DOS) for both Ta-s/d and O-p orbitals shows progressively reduced peak intensities and increased peak broadening, evolving from sharp features to a broadened distribution.

Specifically, regarding hybridization: At $Q_1 = 0$ amu$^{1/2}\cdot$ Å, significant DOS overlap between Ta-d and O-p orbitals occurs within the range of $E \approx 4$ eV–8 eV, indicative of strong hybridization. As Q_1 increases, however, distortions in Ta–O bonds (e.g., altered bond lengths, symmetry breaking) compromise the geometric criteria essential for efficient d–p hybridization. This leads to a marked reduction in hybridization strength, manifested as a diminished DOS overlap region and increased peak dispersion.

3.3. Optical properties

The optical properties of materials, critical for understanding and designing novel materials, are primarily governed by electronic dynamics (e.g., transition probabilities). Using the GW+BSE approach, we analyzed light-induced structural phase transitions in $KTaO_3$ and their impact on key optical parameters: dielectric function (ε), absorption coefficient (α), energy loss function (L), refractive index (n), reflectivity (R), and extinction coefficient (k) (Fig. 5). Pristine $KTaO_3$ exhibits optical trends consistent with prior studies,[55] while pump excitation induces marked alterations in these properties, revealing dynamic light–matter interactions.

The dielectric function $\varepsilon(\omega) = \varepsilon_1(\omega) + \mathrm{i}\varepsilon_2(\omega)$ quantifies a material's response to electric fields, where the real part $\varepsilon_1(\omega)$ governs polarization and the imaginary part $\varepsilon_2(\omega)$ reflects absorption. Key features in $\varepsilon_2(\omega)$ (e.g., spectral peaks and lineshapes) directly correlate with interband electronic transitions. These parameters reveal the material's optical and electronic behavior, governing their performance in applications. For $KTaO_3$, the static $\varepsilon_1(\omega)$ peaks at 9.38 (2.18 eV), while $\varepsilon_1(\omega)$ peaks at 6.68 (4.23 eV), revealing its light–matter interaction thresholds.

The absorption coefficient $\alpha(\omega)$ quantifies a material's photon absorption efficiency. This absorption process is determined by multiple factors, such as the material's band structure and atomic arrangement. Specifically, optical absorption arises when the photon energy equals the energy difference between electronic states in the material. The optical absorption coefficient $\alpha(\omega)$ can be calculated from the imaginary part of the dielectric function $\varepsilon_2(\omega)$

$$\alpha(\omega) = \frac{\sqrt{2}\omega}{c}\left[\sqrt{\varepsilon_1^2+\varepsilon_2^2} - \varepsilon_1\right]^{1/2}. \tag{4}$$

Here, ω represents the photon frequency and c denotes the speed of light in vacuum. A higher absorption coefficient indicates stronger absorption. The absorption coefficient $\alpha(\omega)$ of $KTaO_3$, calculated from the dielectric function (Figs. 5(a) and 5(d)), reveals distinct photon energy dependence: pristine $KTaO_3$ exhibits isotropic absorption onset at 3.5 eV with the first absorption peak appears at 3.88 eV.

Nonlinear phononic coupling induces atomic displacements (Q_1) along the z-axis, breaking structural symmetry and thereby inducing anisotropy in the optical response. Along the [001] direction, the calculated absorption spectra show a clear blueshift of the absorption edge with increasing characteristic displacement Q_1 (Fig. 5(i)). The excitonic absorption peaks at $Q_1 = 0$ amu$^{1/2}\cdot$ Å and $Q_1 = 0.6$ amu$^{1/2}\cdot$ Å are marked in Figs. 5(a). Figures 5(i) and 5(l) present the $\boldsymbol{k}$-space weight distributions of the first excitonic states at $Q_1 = 0$ amu$^{1/2}\cdot$ Å and $Q_1 = 0.6$ amu$^{1/2}\cdot$ Å, respectively. Dot radii represent the contribution strength of valence-to-conduction electron–hole (EH) pairs to the excitonic wavefunction at each $\boldsymbol{k}$-point. At $Q_1 = 0$ amu$^{1/2}\cdot$ Å, the exciton state is dominated by VBM to CBM EH pairs near the Gamma point. At $Q_1 = 0.6$ amu$^{1/2}\cdot$ Å, the primary e-h pairs forming the exciton shift from the Gamma point vicinity toward Brillouin zone regions exhibiting larger band gaps. This shift to higher band gap regions increases the transition energy of the EH pairs, directly resulting in the blueshift of both the excitonic peak and absorption edge. In contrast, the [100] direction shows no significant absorption edge shift, consistent with minimal band gap changes.

The energy loss function $L(\omega)$ is a fundamental tool for studying light–matter interactions. It quantifies electron energy dissipation in electromagnetic fields, representing the probability distribution of energy loss when incident electrons or photons interact with the material. The expression is given as follows:

$$L(\omega) = \mathrm{Im}\left(\frac{-1}{\varepsilon(\omega)}\right) = \frac{\varepsilon_2}{\varepsilon_1^2+\varepsilon_2^2}. \tag{5}$$

The energy loss function $L(\omega)$ of $KTaO_3$ (Figs. 5(b) and 5(e)) highlights plasmonic resonances, with pristine samples showing a prominent bulk plasmon peak at 7.4 eV. As Q_1 displacement changes, along [001] (Fig. 5(b)), the loss threshold blueshifts systematically with suppressed intensity, while along [100] (Fig. 5(e)), loss intensity decreases without spectral shifts. These modifications collectively reduce energy dissipation, indicating enhanced energy transfer efficiency under optical excitation, driven by symmetry-breaking atomic rearrangements

The extinction coefficient $k(\omega)$, a fundamental optical parameter, describes light attenuation in materials through optical amplitude decay. It relates to the absorption coefficient

$\alpha(\omega)$ as

$$k(\omega) = \frac{c\alpha(\omega)}{2\omega} = \left[\frac{\sqrt{\varepsilon_1^2+\varepsilon_2^2}-\varepsilon_1}{2}\right]^{1/2}. \quad (6)$$

Figures 5(c) and 5(f) show the energy dependence of the extinction coefficient. The extinction coefficient of $KTaO_3$ exhibits an onset at 3.5 eV, reaching a pronounced peak value of 1.76 at 4.5 eV where maximal photon absorption occurs at the material surface. This spectral evolution mirrors the imaginary component ($\mathrm{Im}(\varepsilon)$) of the dielectric function, confirming $k(\omega)$ as a critical parameter for optoelectronic device engineering.

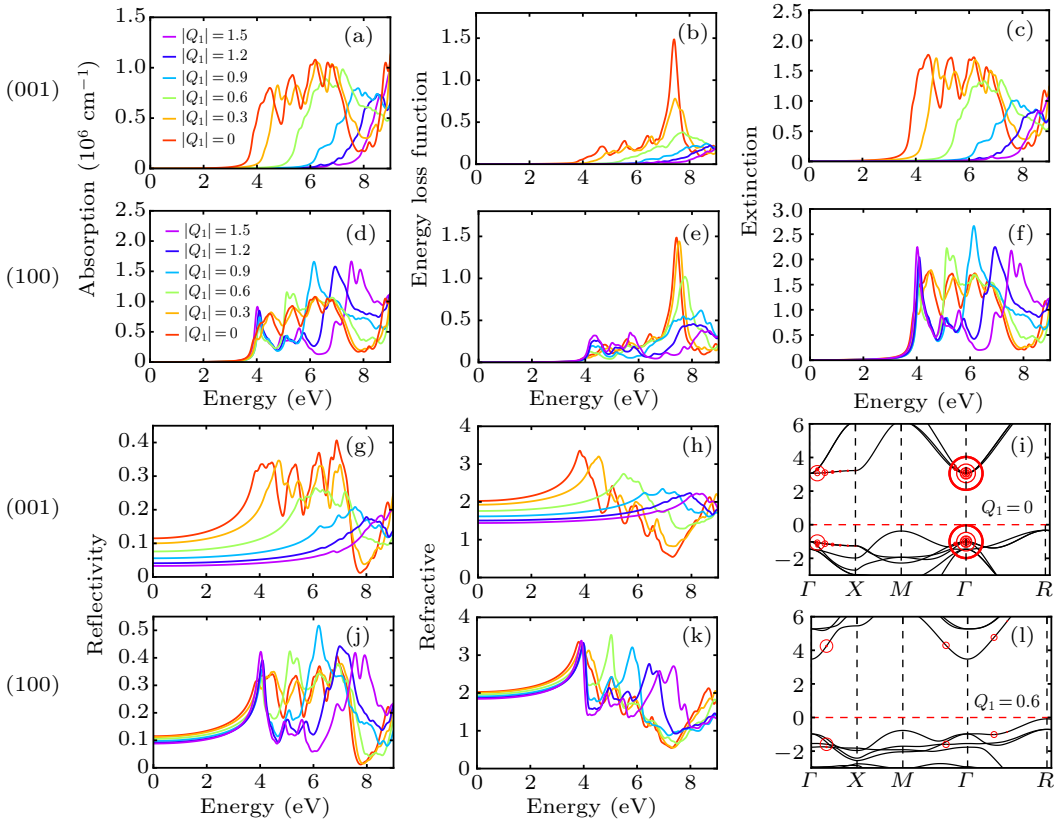


Fig. 5. The calculated panels (a) and (d) absorption coefficient, (b) and (e) energy loss function, (c) and (f) extinction, (g) and (j) reflectivity, and (h) and (k) refractive index for $KTaO_3$. (i) and (l) The band structure near the Γ point (marked by black lines). The radius of the red circle represents the contribution of the EH pair to the exciton wavefunction at that point.

The reflectivity ($R(\omega)$), defined as the ratio of reflected to incident light intensity at a material's surface, represents a fundamental parameter characterizing the light-reflecting capability of materials. It can be expressed as

$$R(\omega) = \frac{(n-1)^2+k^2}{(n+1)^2+k^2} = \left|\frac{\sqrt{\varepsilon(\omega)}-1}{\sqrt{\varepsilon(\omega)}+1}\right|^2. \quad (7)$$

Figures 5(g) and 5(j) show the energy-dependent reflectivity spectra of light excited $KTaO_3$ within the range of 0.0 eV–9.0 eV. For pristine $KTaO_3$, the maximum reflectivity reaches 0.41 at 6.88 eV, which is significantly lower than the corresponding absorption value of 0.734 reported for $KZnO_3$.[55] For light-induced $KTaO_3$, the reflectivity along the [001] direction shows a significant decrease with increasing Q_1 displacement, The static reflectance $R(0)$ decreased from 0.11 to 0.03, representing a 73% reduction. This light-induced reduction in reflectivity suggests potential applications in solar cell designs and optical coatings. The systematic modulation of reflectivity via light-induced highlights the tunable optical properties of $KTaO_3$ for photonic applications.

The refractive index $n(\omega)$ characterizes the propagation behavior of light in a material medium, defined mathematically as

$$n(\omega) = \left[\frac{\sqrt{\varepsilon_1^2+\varepsilon_2^2}+\varepsilon_1}{2}\right]^{1/2}. \quad (8)$$

Figures 5(h) and 5(k) depict the energy dependence of the refractive index $n(\omega)$ for $KTaO_3$ along two crystallographic directions. At 3.82 eV, the refractive index reaches its maximum value of 3.35. The material exhibits a static refractive index $n(0) = 2.02$ at zero energy, close to the 2.31 value calculated by Sarfraz *et al.*[56] $n(0)$ characterizes electron cloud polarization strength under electrostatic fields and directly measures material polarizability. Notably, light-excited reduces $n(0)$ from 2.02 to 1.44 (29% decrease), resulting from light-induced structural modifications that alter atomic arrangements and reduce electronic polarizability. These optically modulated properties link structural dynamics to optical

responses, providing critical guidance for $KTaO_3$-based optoelectronic device engineering.

3.4. Thermodynamic properties

In solids, thermal energy is transported by electrons and phonons. Electronic conduction dominates in metals/semiconductors via free carrier movement, while phonons (lattice vibrations) govern heat transfer in insulators. Phonon-mediated thermal conductivity, reflecting lattice vibration efficiency, critically determines material thermal properties and is pivotal for applications like thermoelectric, thermal barrier coatings, and solid-state refrigeration.[57] At elevated temperatures, phonon contributions intensify. Recent advancements focus on engineering low-thermal-conductivity materials to optimize thermoelectric performance and thermal management systems.

To calculate the lattice thermal conductivity (κ_L), this study employs the framework of the phonon Boltzmann transport equation (BTE) and solves it under the relaxation time approximation (RTA):

$$\kappa_L = \frac{1}{V}\sum_{\lambda} C_\lambda v_\lambda \otimes v_\lambda \tau_\lambda,$$

$$C_\lambda = k_B \left(\frac{\hbar\omega_\lambda}{k_B T}\right)^2 \frac{\exp\left(\hbar\omega_\lambda/(k_B T)\right)}{\left[\exp(\hbar\omega_\lambda/(k_B T)) - 1\right]^2}.$$

Here, λ represents the phonon mode, C_λ is the mode-dependent specific heat capacity, v_λ is the group velocity, and τ_λ is the phonon lifetime.

The phonon dispersion relations and eigenvectors were determined by using the PHONOPY software to process force constants calculated by VASP, yielding phonon frequencies ω_λ and group velocities v_λ. Third-order force constants were computed based on the $2\times2\times2$ supercell. The anharmonic interactions were processed using the phono3py software[58] to characterize the phonon–phonon scattering strength. The phonon lifetime τ_λ is primarily governed by three-phonon scattering processes. The scattering rate was calculated using the phono3py software combined with the third-order anharmonic force constants obtained via the finite displacement method.

The temperature dependence of lattice thermal conductivity is shown in Fig. 6(a), exhibiting characteristic decrease with increasing temperature. Remarkably, modulating the phonon eigenvector Q_1 (from 0 to 0.9 amu$^{1/2}\cdot$Å) induces a 62.9% κ_L reduction at 300 K (from 8.11 W·m^{-1}·K^{-1} to 3.01 W·m^{-1}·K^{-1}, Fig. 6(b)), surpassing the 54% reduction via chemical doping in $KTa_{3-x}S_x$.[35] This demonstrates nonlinear phonon coupling as a superior strategy for thermal conductivity engineering compared to atomic substitution.

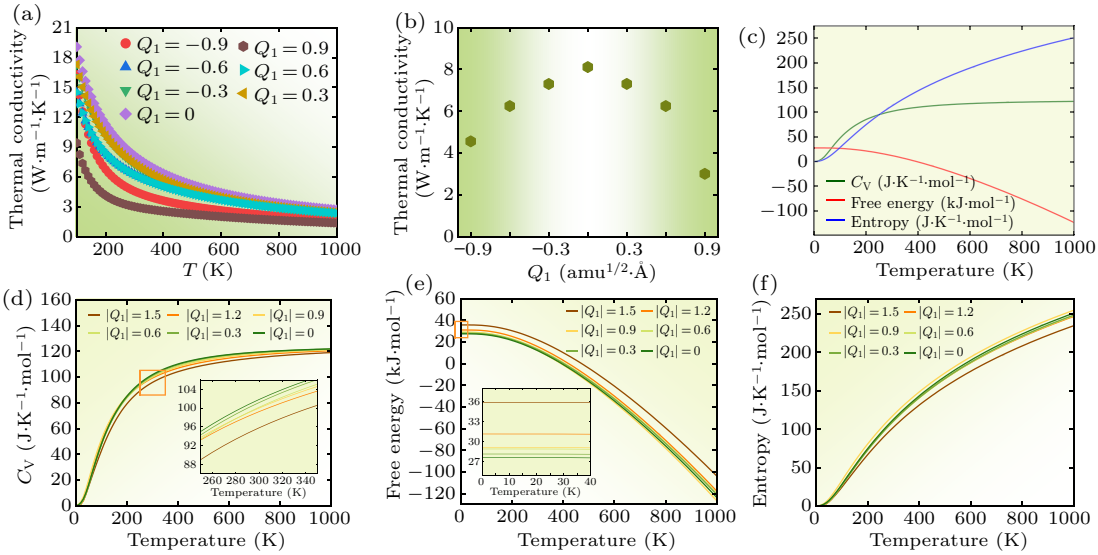


Fig. 6. Calculated thermodynamic properties. (a) The temperature dependence of the lattice thermal conductivity in $KTaO_3$. (b) The calculated lattice thermal conductivity at 300 K. (c) When $Q_1 = 0$ amu$^{1/2}\cdot$Å, the thermodynamic properties of $KTaO_3$ change with temperature. (d) Heat capacity of $KTaO_3$. (e) Free energy of $KTaO_3$. (f) Entropy of $KTaO_3$.

To investigate the microscopic mechanism behind the reduction of lattice thermal conductivity, we calculated the lifetimes of phonons across different frequencies. Research indicates that low-frequency phonons (particularly acoustic phonons) contribute most significantly to thermal conductivity due to their higher group velocities and longer lifetimes, serving as the primary carriers for heat transport. Consequently, changes in the lifetimes of low-frequency phonons exert a dominant influence on thermal conductivity. As shown in Fig. 7, phonon lifetimes decrease markedly with increasing characteristic displacement Q. This phenomenon arises from positional disorder induced by light-driven structural distortions, which enhances phonon scattering intensity. According to the lattice thermal conductivity formula, the reduction in phonon lifetime directly correlates with the decline in thermal conductivity, establishing it as the dominant factor. The reduction in thermal conductivity indicates diminished heat conduction capability in the material, significantly affecting its ther-

mal management performance and potential applications.

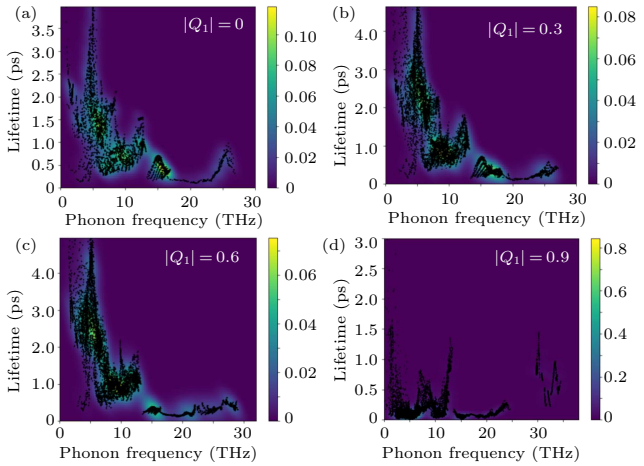


Fig. 7. Calculated phonon lifetime τ, where panels (a), (b), (c), (d), correspond to Q_1 values of 0, 0.3, 0.6, 0.9 amu$^{1/2}\cdot$Å, respectively.

We calculated the Gibbs free energy (G), entropy (S), and heat capacity (C_V), as shown in the following equations:

$$G(T) = E_0 + \int_0^\infty \left[\frac{\hbar\omega}{2} + k_B T \ln(1 - e^{-\hbar\omega/(k_B T)})\right] \times g(\omega)\,d\omega, \quad (9)$$

$$S(T) = -k_B \int_0^\infty \left[\ln(1 - e^{-\hbar\omega/(k_B T)}) - \frac{\hbar\omega/(k_B T)}{(e^{\hbar\omega/(k_B T)} - 1)^2}\right] g(\omega)\,d\omega, \quad (10)$$

$$C_V(T) = k_B \int_0^\infty \left(\frac{\hbar\omega}{k_B T}\right)^2 \frac{e^{\hbar\omega/(k_B T)}}{(e^{\hbar\omega/(k_B T)} - 1)^2} g(\omega)\,d\omega, \quad (11)$$

where E_0 denotes the ground state energy, $g(\omega)$ represents the phonon density of states, $\hbar$ is the reduced Planck constant, k_B is the Boltzmann constant, and T is the temperature. Figure 6(c) displays the temperature dependence of the free energy, entropy, and heat capacity in the primitive unit cell. Heat capacity, a key determinant of lattice thermal conductivity, exhibits an inverse correlation with Q_1 displacement at 300 K (Fig. 6(d)): larger Q_1 values reduce heat capacity, enhancing sensitivity to thermal perturbations. Free energy universally decreases with rising temperature (Fig. 6(e)), confirming thermodynamic stability. Entropy peaks at $|Q_1| = 0.9$ amu$^{1/2}\cdot$Å and minimizes at $|Q_1| = 1.5$ amu$^{1/2}\cdot$Å (Fig. 6(f)), demonstrating displacement-dependent disorder modulation. These coordinated responses highlight how nonlinear phonon coupling governs both thermal transport and thermodynamic stability in engineered $KTaO_3$.

Reducing κ_L suppresses heat diffusion, significantly decreasing thermal loss in devices and thereby improving energy conversion efficiency and extending lifetime. Conventional thermoelectric optimization faces challenges: nanostructuring suppresses κ_L via enhanced phonon scattering but degrades carrier mobility through interface scattering; chemical doping optimizes carrier concentration yet often sacrifices the power factor due to ionized impurity scattering or band distortion. In this study, light-induced nonlinear phonon coupling modulates κ_L by enhancing lattice anharmonicity to selectively shorten phonon lifetime without introducing defects or impurities, thus preserving electronic transport. Given $KTaO_3$'s intrinsically high Seebeck coefficient ($|S| > 150$ μV/K[58]) and photo-induced low κ_L (~ 3.0 W·m^{-1}·K^{-1}), its thermoelectric figure of merit may surpass conventional limits via light-phonon synergy, enabling optically controlled dynamic thermoelectric conversion. In practical application, within a thermoelectric generator, utilizing pulsed lasers to dynamically modulate the material's thermal conductivity in real-time allows for the optimization of the temperature difference between the hot and cold ends. Unlike static traditional methods (alloying/nanocomposites), this light-control mechanism provides a dynamic, non-contact pathway for thermoelectric optimization.

4. Conclusions

This study explores nonlinear coupling between the infrared-active phonon modes TO_1 and TO_2 in $KTaO_3$. Specific pump pulses induced symmetry breaking, exciting the TO_1 mode significantly. Modulating its characteristic displacement coordinate (Q_1) effectively induced structural modifications, regulating the material's optical and thermodynamic properties.

When Q_1 increased from 0 to 1.5 amu$^{1/2}\cdot$Å, band degeneracy lifting occurred at both the Γ and R points. Meanwhile, the [001] direction absorption edge exhibited a blue shift, with reduced energy loss, reflectivity, and refractive index. As Q_1 rose from 0 to 0.9 amu$^{1/2}\cdot$Å, the lattice thermal conductivity decreased from 8.11 W·m^{-1}·K^{-1} to 3.01 W·m^{-1}·K^{-1} (a 62.9% reduction).

This work investigates the mechanism for modulating nonlinear phonon coupling and structural distortions via optical field intensity. It suggests a light-driven approach for dynamically modifying $KTaO_3$'s structure, electronic bands, optical response, and thermal transport. The regulation involves light-enhanced lattice potential anharmonicity through nonlinear phonon coupling, selectively shortening phonon lifetime (τ). This enables thermal conductivity modulation without chemical impurities or static defects, and maintains electronic transport stability. The achieved low thermal conductivity may facilitate larger temperature gradients in thermoelectric devices, potentially improving energy conversion efficiency. The non-contact, real-time tunable optical field could enable dynamic optimization of thermal transport. These findings offer insights for studying photo-thermal coupling and other properties in $KTaO_3$. The light-driven strategy may also inform the design of material platforms for dielectric, optoelectronic,

and sensing applications, particularly for optical devices and controlled modulation of multifunctional materials.

Acknowledgement

Project supported by the National Key Research and Development Program of China (Grant No. 2024YFF0508503)

References

[1] Tkach A, Almeida A, Levin I, Woicik J C and Vilarinho P M 2021 *Materials* **14** 4632
[2] Alexander A, Reticcioli M, Albons L, Redondo J, Corrias M, Píš I, Wang Z, Johánek V, Mysliveček J, Franchini C, Wrana D and Setvin M 2024 *ACS Appl. Mater. Interfaces* **16** 70010
[3] Vikhnin V, Eden S, Aulich M and Kapphan S 2000 *Solid State Commun.* **113** 455
[4] Kim M J, Kovalev S, Udina M, Haenel R, Kim G, Puviani M, Cristiani G, Ilyakov I, de Oliveira T V A G, Ponomaryov A, Deinert J C, Logvenov G, Keimer B, Manske D, Benfatto L and Kaiser S 2024 *Sci. Adv.* **10** eadi7598
[5] Wang E, Adelinia J D, Chavez-Cervantes M, Matsuyama T, Fechner M, Buzzi M, Meier G and Cavalleri A 2023 *Nat. Commun.* **14** 7233
[6] Katsumi K, Nishida M, Kaiser S, Miyasaka S, Tajima S and Shimano R 2023 *Phys. Rev. B* **107** 214506
[7] Tang R and Zhang H 2025 *Opt. Express* **33** 5900
[8] Pfaff C, Pezeril T, Arras R, Calmels L, Cherruault V, Andrieu S, Dumesnil K, Gorchon J and Hauet T 2025 *Phys. Rev. B* **111** 064405
[9] Kogar A, Zong A, Dolgirev P E, Shen X, Straquadine J, Bie Y-Q, Wang X, Rohwer T, Tung I C, Yang Y, Li R, Yang J, Weathersby S, Park S, Kozina M E, Sie E J, Wen H, Jarillo-Herrero P, Fisher I R, Wang X and Gedik N 2020 *Nat. Phys.* **16** 159
[10] Zhang J, Lian C, Guan M, Ma W, Fu H, Guo H and Meng S 2019 *Nano Lett.* **19** 6027
[11] Tang R, Boi F and Cheng Y H 2023 *npj Quantum Mater.* **8** 78
[12] Guan M X, Wang E, You P W, Sun J T and Meng S 2021 *Nat. Commun.* **12** 1885
[13] Shin D, Sato S A, Hübener H, De Giovannini U, Park N and Rubio A 2020 *npj Comput. Mater.* **6** 182
[14] Völkel A, Nimmesgern L, Mielnik-Pyszczorski A, Wirth T and Herink G 2022 *Nat. Commun.* **13** 2066
[15] Mitrano M, Cantaluppi A, Nicoletti D, Kaiser S, Perucchi A, Lupi S, Di Pietro P, Pontiroli D, Riccò M, Clark S R, Jaksch D and Cavalleri A 2016 *Nature* **530** 461
[16] Cantaluppi A, Buzzi M, Jotzu G, Nicoletti D, Mitrano M, Pontiroli D, Riccò M, Perucchi A, Di Pietro P and Cavalleri A 2018 *Nat. Phys.* **14** 837
[17] Rowe E, Yuan B, Buzzi M, Jotzu G, Zhu Y, Fechner M, Först M, Liu B, Pontiroli D, Riccò M and Cavalleri A 2023 *Nat. Phys.* **19** 1821
[18] Sie E J, Nyby C M, Pemmaraju C D, Park S J, Shen X, Yang J, Hoffmann M C, Ofori-Okai B K, Li R, Reid A H, Weathersby S, Mannebach E, Finney N, Rhodes D, Chenet D, Antony A, Balicas L, Hone J, Devereaux T P, Heinz T F, Wang X and Lindenberg A M 2019 *Nature* **565** 61
[19] Vaswani C, Wang L L, Mudiyanselage D H, Li Q, Lozano P M, Gu G D, Cheng D, Song B, Luo L, Kim R H J, Huang C, Liu Z, Mootz M, Perakis I E, Yao Y, Ho K M and Wang J 2020 *Phys. Rev. X* **10** 021013
[20] McIver J W, Schulte B, Stein F U, Matsuyama T, Jotzu G, Meier G and Cavalleri A 2020 *Nat. Phys.* **16** 38
[21] Zhu J, Pan Z, Xiong J and Wu X 2025 *Phys. Scr.* **100** 035525
[22] Abalmasov V A 2020 *Phys. Rev. B* **101** 014102
[23] Yang Q and Meng S 2024 *Phys. Rev. Lett.* **133** 136902
[24] Kahana T, Bustamante Lopez D A and Juraschek D M 2024 *Sci. Adv.* **10** eado0722
[25] Li X, Qiu T, Zhang J, Baldini E, Lu J, Rappe A M and Nelson K A 2019 *Science* **364** 1079
[26] Shin D, Latini S, Schäfer C, Sato S A, Baldini E, De Giovannini U, Hübener H and Rubio A 2022 *Phys. Rev. Lett.* **129** 167401
[27] Subedi A, Cavalleri A and Georges A 2014 *Phys. Rev. B* **89** 220301
[28] Juraschek D M and Maehrlein S F 2018 *Phys. Rev. B* **97** 174302
[29] Först M, Manzoni C, Kaiser S, Tomioka Y, Tokura Y, Merlin R and Cavalleri A 2011 *Nat. Phys.* **7** 854
[30] Först M, Tobey R I, Wall S, Bromberger H, Khanna V, Cavalieri A L, Chuang Y D, Lee W S, Moore R, Schlotter W F, Turner J J, Krupin O, Trigo M, Zheng H, Mitchell J F, Dhesi S S, Hill J P and Cavalleri A 2011 *Phys. Rev. B* **84** 241104
[31] Först M, Mankowsky R, Bromberger H, Fritz D M, Lemke H, Zhu D, Chollet M, Tomioka Y, Tokura Y, Merlin R, Hill J P, Johnson S L and Cavalleri A 2013 *Solid State Commun.* **169** 24
[32] Först M, Mankowsky R and Cavalleri A 2015 *Acc. Chem. Res.* **48** 380
[33] Disa A S, Nova T F and Cavalleri A 2021 *Nat. Phys.* **17** 1087
[34] Wang J, You J L, Wang X P, Wang M, Zhang Q L, Wan S M and Lu L M 2022 *J. Mol. Liq.* **365** 120098
[35] Jawad M, Rahman A U, Mirza S H, Azam S, Amin N U, Amin M A and El-Bahy S M 2024 *J. Phys. Chem. Solids* **194** 112213
[36] Blöchl P E 1994 *Phys. Rev. B* **50** 17953
[37] Kresse G and Hafner J 1994 *Phys. Rev. B* **49** 14251
[38] Kresse G and Furthmüller J 1996 *Comput. Mater. Sci.* **6** 15
[39] Kresse G and Furthmüller J 1996 *Phys. Rev. B* **54** 11169
[40] Perdew J P, Burke K and Ernzerhof M 1996 *Phys. Rev. Lett.* **77** 3865
[41] Grimme S, Antony J, Ehrlich S and Krieg H 2010 *J. Chem. Phys.* **132** 154104
[42] Togo A and Tanaka I 2015 *Scr. Mater.* **108** 1
[43] Heyd J, Scuseria G E and Ernzerhof M 2003 *J. Chem. Phys.* **118** 8207
[44] Onida G, Reining L and Rubio A 2002 *Rev. Mod. Phys.* **74** 601
[45] Salpeter E E and Bethe H A 1951 *Phys. Rev.* **84** 1232
[46] Togo A 2022 *J. Phys. Soc. Jpn.* **92** 012001
[47] Uwe H and Sakudo T 1977 *Phys. Rev. B* **15** 337
[48] Goulielmakis E and Brabec T 2022 *Nat. Photon.* **16** 411
[49] Chen J, Xia Q and Fu L 2021 *Phys. Rev. A* **104** 063109
[50] Kato H and Kudo A 2001 *J. Phys. Chem. B* **105** 4285
[51] Wu B, Cai J and Zhou X 2022 *RSC Adv.* **12** 32270
[52] Li H Y, Mu Z, Liu Z T, Du Y H and Liu Q J 2022 *Physica B* **647** 414372
[53] Akter H, Hossain M M, Uddin M M, Naqib S H and Ali M A 2024 *J. Phys. Chem. Solids* **190** 112021
[54] Zhu Q, Chen J, Gou G, Chen H and Li P 2017 *J. Mater. Process. Technol.* **246** 267
[55] Hussain S and Rehman J U 2024 *Physica B* **687** 416116
[56] Sarfraz S, Aldaghfag S A, Butt M K, Yaseen M, Zahid M and Dahshan A 2022 *Mater. Sci. Semicond. Process.* **148** 106811
[57] Naher M I and Naqib S H 2022 *Results Phys.* **37** 105505
[58] Himmetoglu B and Janotti A 2016 *J. Phys. Condens. Matter* **28** 065502